A novel three-dimensional, two-phase and non-isothermal numerical model for proton exchange membrane fuel cell

Chun-Hua Min*

School of Energy and Environmental Engineering, Hebei University of Technology, Tianjin 300401, PR China

ARTICLE INFO

ABSTRACT

A three-dimensional, two-phase and non-isothermal model of a proton exchange membrane fuel cell (PEMFC) based on the previously developed model is established using the two-fluid method. This two-phase model considers the liquid water transport in both cathode and anode sides and accounts for the intrinsic heat transfer between the reactant fluids and the solid matrices. The latent heat of water condensation/evaporation is considered in the present model. The numerical results demonstrate that the lower cathode humidity is beneficial for cell performance. In the anode side, the water vapor can be condensed at high current density because the water vapor transport is less than the hydrogen consumption rate. Near the catalyst layer, the reactant fluid temperature is higher than the solid matrix temperature, and far from the catalyst layer, the temperature difference between the reactant fluid and the solid matrix decreases. Near the channel, the reactant fluid temperature is lower than the solid matrix temperature.

1. Introduction

The proton exchange membrane fuel cell (PEMFC) is considered a promising alternative power source for future automobiles and stationary applications owing to its high-energy efficiency, competitive power density, low-temperature operation, fast start-up and pollution-free characteristic. However, the performance of the PEMFCs needs to be further improved to increase their cost-effectiveness so that they can compete against the traditional combustion engines [1]. Water management is a key issue in PEM-FCs, and is a significant technical challenge. On the one hand, sufficient water is needed in the membrane to maintain sufficiently high proton conductivity, but on the other hand, excess liquid water in the electrode can cause water flooding, and hinder the transport of the reactant from the gas channel to the catalyst layer. To optimize water management, some two-phase models have been presented. He et al. [1] developed a 2D and two-phase model of water transport in the cathode diffusion layer (GDL). They introduced an equation for liquid water transport which accounted for the shear force of gas flow and capillary force. Siegel et al. [2] assumed that the liquid phase had the same velocity with the gas phase. Liu and coworkers [3,4] and Hu and Fan [5] employed mixture models for two-phase behavior in PEMFCs. Wang et al. [6] also presented a mixture model to describe the two-phase behavior in a PEMFC. They predicted that the liquid water saturation within the cathode will reach 6.3% at 1.4 A cm^{-2} for dry inlet air. Chen et al. [7] also presented a mixture model to investigate the transport characteristics in the cathode GDL of a PEMFC with a gradient in porosity. The results demonstrated that a gradient in porosity will benefit the removal rate of liquid water. Tao et al. [8,9], He et al. [10] and Meng [11] all developed two-fluid models, in which a parameter, liquid water saturation, is used to describe the liquid water transport.

The above discussed literatures mainly focus on the liquid water transport in the cathode side. Actually, the liquid water is often generated in the anode side by condensation [12]. In our present work, the water vapor condensation in the anode was modeled which is the continuation of our previous work [13]. The single-phase model was further extended to consider liquid water transport based on a traditional two-fluid model.

2. Model description

A schematic view of a PEMFC with parallel flow fields and computational domain is shown in Fig. 1. It is assumed that the PEMFC structure is repeated periodically along the y-direction. To save computational time, a typical unit shown in the figure is taken as the computational domain. Humidified hydrogen is fed into the anode channel, whereas air with various relative humidity is fed into the cathode channel. In fact, the relative humidity of the air is a factor affecting PEMFC performance that is analyzed in the following sections.

The assumptions adopted in the present model are as follows:

(1) The fuel cell operates under steady-state condition.
(2) The gas mixture is an incompressible ideal fluid.

* Tel.: +86 22 60204525; fax: +86 22 60204530.
  E-mail addresses: chmin@hebut.edu.cn, minchunhua@163.com.

Nomenclature

A	area (m^2)
A_s	specific area of the catalyst layer (m^{-1})
a	water activity
C	molar concentration ($mol\,m^{-3}$)
D	diffusion coefficient ($m^2\,s^{-1}$)
E	equilibrium thermodynamic potential (V)
F	Faraday constant ($96487\,C\,mol^{-1}$)
f	relative consumption rate of hydrogen and water vapor transport
H	height (m)
h_v	interfacial heat transfer coefficient ($W\,m^3\,K^{-1}$)
i	reaction rate ($A\,m^{-3}$)
I	current density ($A\,m^{-2}$)
K	permeability (m^2)
k	thermal conductivity ($W\,(m\,K)^{-1}$)
k_{con}	condensation rate coefficient (s^{-1})
k_{evp}	evaporation rate coefficient ($s^{-1}\,Pa^{-1}$)
L	length (m)
M	molar mass ($kg\,mol^{-1}$)
n	electron number for electrochemical reactions
n_d	electro-osmotic drag coefficient
p	pressure (Pa)
R	resistance ($\Omega\,cm^2$); gas constant ($8.314\,J\,mol^{-1}\,K^{-1}$)
RH	relative humidity
r_w	latent heat of phase change ($J\,kg^{-1}$)
S	source term
T	temperature (K)
$\mathbf{u}$	velocity vector ($m\,s^{-1}$)
V	voltage (V)
W	width (m)
x, y, z	coordinate direction (m)
X	molar fraction

Greek symbols

α	transfer coefficient
β	net water transfer rate
ε	porosity
η	overpotential (V)
κ	conductivity ($S\,m^{-1}$)
λ	membrane water content
μ	fluid viscosity ($kg\,m^{-1}\,s^{-1}$)
ρ	density of the fluid ($kg\,m^{-3}$)
σ	surface tension ($N\,m^{-1}$)
ω	mass fraction
ζ	stoichiometric ratio

Subscripts and superscripts

0	before the diffusion layer
a	anode
act	activation
av	average
c	cathode or capillary
cc	current collector
conc	concentration
ct	catalyst layer
cell	fuel cell
ch	channel
d	diffusion layer
eff	effective value
el	electron transfer
g	gas phase
in	inlet channel
i	species

int	interfacial value
L	limiting
l	liquid
m	mass or membrane
ohm	ohmic polarization
pro	ion transfer
r	relative values
ref	reference
s	specific or solid phase
T	temperature
w	water

Superscript

sat	saturation

(3) The gas flow in the channels is laminar.

(4) All the porous zones in the fuel cell domain are assumed to be isotropic and homogeneous, and the membrane is considered impervious to reactant gases.

(5) Ohmic heating in the bipolar plates and the diffusion layers are neglected due to their high conductivities.

(6) The gas and liquid phases in the fuel cell exist as continuous phases.

2.1. Governing equations

The three-dimensional, two-phase, non-isothermal model consists of non-linear, coupled partial differential equations representing the conservation of mass, momentum, species, energy and liquid water. Correlations for the capillary pressure and the saturation level connect the two-fluid transports. The interactions between the reactant fluid and solid matrix temperatures are accounted with a non-isothermal model, in which the irreversibility heating due to electrochemical reactions, Joule heating arising from ohmic resistance and latent heat of water condensation/evaporation are considered. The conservation equations are described in vector form as follows.

2.1.1. Continuity equations

The continuity equations for gas mixture and liquid water are described by

$$\nabla \cdot (\rho_g \mathbf{u}_g) = S_m = \begin{cases} S_{H_2} + S_w & \text{Anode} \\ S_{O_2} + S_w - S_{phase} & \text{Cathode} \end{cases}, \quad (1)$$
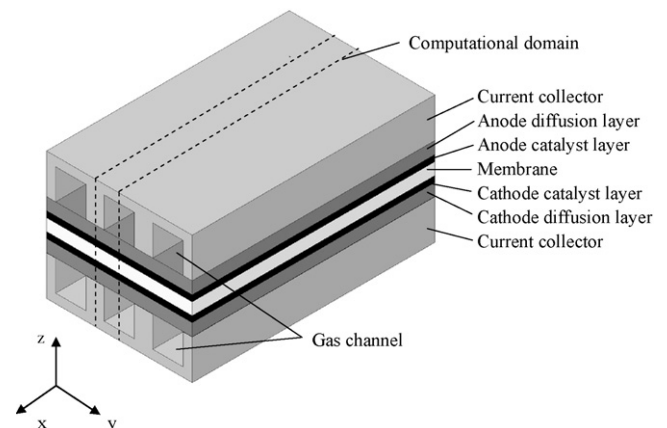

Fig. 1. Schematic view of a PEMFC.

$$\nabla \cdot (\rho_l \boldsymbol{u}_l) = S_{\text{phase}}, \tag{2}$$

where ρ_g and ρ_l are the densities of gas mixture and liquid water, respectively. u_g and u_l are the velocities of gas mixture and liquid water, respectively. S_{H_2}, S_{O_2} and S_w denote the source terms due to electrochemical reactions in the catalyst layers of hydrogen, oxygen and water vapor, respectively. In the present two-phase model, water produced in the cathode catalyst layer is assumed to be in vapor phase. This is different from the assumption made in [1,14], but it should make no difference in the final results since water vapor and liquid water would approach their thermodynamic equilibrium conditions through condensation/evaporation processes [11]. The source terms are determined by

$$S_{H_2} = \frac{-i_a}{2F} M_{H_2}, \tag{3}$$

$$S_{O_2} = \frac{-i_c}{4F} M_{O_2}, \tag{4}$$

$$S_w = \begin{cases} (-\beta i_a/F) M_{H_2O} & \text{Anode} \\ \dfrac{(1+2\beta) i_c}{2F} M_{H_2O} & \text{Cathode} \end{cases}. \tag{5}$$

The interfacial mass transfer rate of water between the gas and liquid phases, S_{sphase}, is expressed as

$$S_{\text{phase}} = \begin{cases} k_{\text{con}} \varepsilon (1-s) X_w \dfrac{(p_{H_2O} - p_{H_2O}^{\text{sat}})}{RT} & p_{H_2O} - p_{H_2O}^{\text{sat}} \geq 0 \\ k_{\text{evp}} \varepsilon s \dfrac{\rho_w}{M_{H_2O}} (p_{H_2O} - p_{H_2O}^{sat}) & p_{H_2O} - p_{H_2O}^{sat} < 0 \end{cases}. \tag{6}$$

The upper form represents the condensation rate while the lower form represents the evaporation rate. k_{con} and k_{evp} are the condensation and evaporation rate coefficients, respectively [1]. X_w is the mole fraction of water vapor. $p_{H_2O}^{\text{sat}}$ is the saturation pressure of water at operating temperature (T_f) which is given by [11]:

$$\log_{10} p_{H_2O}^{\text{sat}} = -2.1794 + 0.02593 T_f - 9.1837 \times 10^{-5} T_f^2$$
$$+ 1.4454 \times 10^{-7} T_f^3. \tag{7}$$

2.1.2. Momentum equations

The momentum equation for gas mixture is expressed as

$$\frac{1}{\varepsilon^2 (1-s)^2} \nabla \cdot (\rho_g \boldsymbol{u}_g \boldsymbol{u}_g) = -\nabla p_g + \frac{1}{\varepsilon (1-s)} \nabla \cdot (\mu_g \nabla \boldsymbol{u}_g) + \frac{\mu_g}{K K_{rg}} \boldsymbol{u}_g. \tag{8}$$

In porous medium region, the general momentum conservation equation reduces to the expression of Darcy's law due to the lower velocities [8], i.e.:

$$\boldsymbol{u}_g = -\frac{K K_{rg}}{\mu_g} \nabla p_g, \tag{9}$$

$$\boldsymbol{u}_l = -\frac{K K_{rl}}{\mu_l} \nabla p_l, \tag{10}$$

where K is the absolute permeability of the electrode, while K_{rg} and K_{rl} are the relative permeabilities of gas mixture and liquid water, respectively, and are represented by $K_{rg} = (1-s)^3$ and $K_{rl} = s^3$. The parameter, s, is the liquid water saturation, defined as the volume fraction of liquid water in the porous media. The liquid water pressure is defined as

$$p_l = p_g - p_c. \tag{11}$$

The capillary pressure p_c, is assumed to be a function of liquid water saturation [11]:

$$p_c = \sigma \left(\frac{\varepsilon}{K} \right)^{1/2} [1.417(1-s) - 2.12(1-s)^2 + 1.263(1-s)^3], \tag{12}$$

where σ is the surface tension of liquid water.

With Eqs. (1), (2), (9), (10) and (12) the liquid water saturation equation can be derived, which says

$$\nabla \cdot \left(\rho_l \frac{\mu_g}{\mu_l} \frac{K_{rl}}{K_{rg}} \boldsymbol{u}_g \right) + \nabla \cdot (\rho_l D_c \nabla s) = S_{\text{phase}}, \tag{13}$$

where D_c is the capillary diffusion coefficient, and is expressed as

$$D_c = \frac{K K_{rl}}{\mu_l} \frac{\mathrm{d} p_c}{\mathrm{d} s}. \tag{14}$$

2.1.3. Species conservation equations

The model accounts for three species in the PEMFC, i.e., hydrogen, oxygen, and water vapor. The conservation equations are given by

$$\nabla \cdot (\rho \boldsymbol{u}_g \omega_{H_2}) = \nabla \cdot (\rho D_{H_2,\text{eff}} \nabla \omega_{H_2}) + S_{H_2}, \tag{15}$$

$$\nabla \cdot (\rho \boldsymbol{u}_g \omega_{O_2}) = \nabla \cdot (\rho D_{O_2,\text{eff}} \nabla \omega_{O_2}) + S_{O_2}, \tag{16}$$

$$\nabla \cdot (\rho_g \boldsymbol{u}_g \omega_w) = \nabla \cdot (\rho_g D_{w,\text{eff}} \nabla \omega_w) + S_w, \tag{17}$$

where ω_{H_2}, ω_{O_2} and ω_w are the mass fractions of hydrogen, oxygen and water vapor in the gas mixtures, respectively; $D_{i,\text{eff}}$ is the effective diffusion coefficient of species i in the porous electrode, and is determined by the Bruggeman model [8]:

$$D_{i,\text{eff}} = D_{i,\text{ref}} [\varepsilon (1-s)]^{1.5} \left(\frac{T}{T_{\text{ref}}} \right)^{3/2} \left(\frac{p_{\text{ref}}}{p} \right), \tag{18}$$

where $D_{i,\text{ref}}$ is the reference value at T_{ref} and p_{ref}.

2.1.4. Energy equations

The energy equations for solid matrices and gas mixture in diffusion layers are, respectively, represented by [15]:

$$\nabla \cdot (k_{s,\text{eff}} \nabla T_s) = S_{\text{int}}, \tag{19}$$

$$(\rho c_p)_f \boldsymbol{u} \cdot \nabla T_f = \nabla \cdot (k_{f,\text{eff}} \nabla T_f) - S_{\text{int}} + r_w S_{\text{phase}}, \tag{20}$$

where $k_{s,\text{eff}}$ and $k_{f,\text{eff}}$, are the effective thermal conductivities of solid matrices and reactant fluids, respectively. The product of r_w and S_{phase} stands for the phase change heat transfer. The source term S_{int} refers to the intrinsic heat transfer between the solid matrices and the reactant fluids which can be expressed as

$$S_{\text{int}} = h_v (T_f - T_s). \tag{21}$$

In the catalyst layer, the electrochemical reaction takes place at the interface of reactant fluid and catalyst under a fixed temperature. Therefore, the reactant fluids and the solid matrices have the same temperature [15]:

$$T_s = T_f, \tag{22}$$

$$(\rho c_p)_f \boldsymbol{u} \cdot \nabla T_f = \nabla \cdot (k_{c,\text{eff}} \nabla T_f) + S_{T,f}, \tag{23}$$

where $k_{c,\text{eff}}$ is the effective thermal conductivity of the catalyst layer. The source term, $S_{T,f}$, is described by

$$S_{T,f} = \eta_{\text{act}} i + \frac{I_m}{\kappa_m} + r_w S_{\text{phase}}, \tag{24}$$

where η_{act} is the activation overpotential, I_m the local current density and κ_m the membrane phase electrical conductivity.

In the membrane, the heat transfer by the liquid water is neglected and the membrane is considered as a heat-conducting solid [16]. The governing equation is described by

$$\nabla \cdot (k_{m,\text{eff}} \nabla T_m) + S_{T,m} = 0, \tag{25}$$

where $k_{m,eff}$, is the effective thermal conductivity of the membrane. The source term, $S_{T,m}$, is described by

$$S_{T,m} = \frac{I_m}{\kappa_m}. \tag{26}$$

The local current density inside the membrane is obtained by [17]:

$$\nabla I_m = \begin{cases} -i_a & \text{Anode catalyst layer} \\ 0 & \text{Membrane} \\ i_c & \text{Cathode catalyst layer} \end{cases}. \tag{27}$$

2.1.5. Water transport in the membrane

When electrochemical reaction occurs in the fuel cells, protons move from anode to cathode through the membrane with water molecules. This process is called electro-osmotic drag. Additionally, some product water transports from cathode to anode due to concentration gradient, which is called back diffusion. Hence, the amount of water transport from anode to cathode is equal to the difference between the amount of water by back diffusion and that by electro-osmotic drag [18].

To minimize the complexity of the model, it is assumed that the gradient of water concentration across the membrane can be approximated by a single-step linear difference between the concentration at the cathode and anode, and the final expression of net water transport coefficient per proton can be described by

$$\beta = \frac{n_d - FD_w(C_{w,c} - C_{w,a})}{I_m H_m}, \tag{28}$$

where $C_{w,a}$ and $C_{w,c}$ represent the molar concentration of water on the anode and cathode, respectively. H_m is the membrane height. n_d and D_w are the electro-osmotic coefficient and diffusion coefficient, respectively, and can be calculated as function of water content, λ, in the membrane based on the correlations by

$$n_d = 0.0029\lambda^2 + 0.05\lambda - 3.4 \times 10^{-19}, \tag{29}$$

$$D_w = 5.5 \times 10^{-11} n_d \exp\left[2416 \times \left(\frac{1}{303} - \frac{1}{T}\right)\right]. \tag{30}$$

The molar concentration of water on the anode and cathode sides, $c_{w,a}$ and $c_{w,c}$, can be obtained from [19]:

$$C_{w,k} = \frac{\rho_{m,dry}}{M_{m,dry}}\lambda, \tag{31}$$

where $\rho_{m,dry}$ is the dry membrane material density; $M_{m,dry}$ is the equivalent weight of the dry membrane; the subscript k denotes a or c for anode/cathode side, respectively. The water content λ in the membrane is given by

$$\lambda = \begin{cases} 0.043 + 17.81a - 39.85a^2 + 36.0a^3 & 0 < a \leq 1 \\ 14 + 1.4(a - 1) & 1 \leq a \leq 3 \end{cases}, \tag{32}$$

where a is the activity of water and can be expressed as

$$a = \frac{x_w p}{p_{H_2O}^{sat}}. \tag{33}$$

The membrane phase conductivity is a function of temperature and water content and is given by

$$\kappa_m = (0.5319\lambda - 0.326)\exp\left[1268\left(\frac{1}{303} - \frac{1}{T}\right)\right]. \tag{34}$$

2.1.6. Electrochemical reactions

The cell voltage is obtained by subtracting all overpotential values from the equilibrium thermodynamic potential as follows:

$$V_{cell} = E - \eta_{act} - \eta_{ohm} - \eta_{conc}, \tag{35}$$

where E is the equilibrium thermodynamic potential, and can be calculated using the Nernst equation [8]:

$$E = 1.23 - 0.9 \times 10^{-3}(T - 298) + 2.3\frac{RT}{4F}\log(p_{H_2}^2 p_{O_2}). \tag{36}$$

η_{act} is the activation overpotential, η_{ohm} is the ohmic overpotential and η_{conc} is the concentration overpotential. These parameters have been discussed in Ref. [13]:

(1) Activation overpotential

The activation overpotential comprises anode and cathode contributions and is expressed by the Bulter–Volmer equation:

$$i_a = A_s i_{a,ref}\left(\frac{C_{H_2}}{C_{H_2,ref}}\right)^{1/2}$$
$$\times \left\{\exp\left[\frac{\alpha_a n_a F}{RT}\eta_{act,a}\right] - \exp\left[-\frac{(1 - \alpha_a)n_a F}{RT}\eta_{act,a}\right]\right\}, \tag{37}$$

$$i_c = A_s i_{c,ref}\frac{C_{O_2}}{C_{O_2,ref}}$$
$$\times \left\{\exp\left[-\frac{\alpha_c n_c F}{RT}\eta_{act,c}\right] - \exp\left[\frac{(1 - \alpha_c)n_c F}{RT}\eta_{act,c}\right]\right\}, \tag{38}$$

where C denotes the molar concentration of reactants. The relationship between the molar concentration and the mass fraction can be expressed as

$$C = \frac{\rho_g \omega}{M}. \tag{39}$$

(2) Ohmic overpotential

The ohmic overpotential comprises contributions from the resistance to electron transfer and to ion transfer. Based on Ohm's law, it can be expressed as

$$\eta_{ohm} = \eta_{ohm}^{el} + \eta_{ohm}^{pro} = I(R^{el} + R^{pro}). \tag{40}$$

where R^{el} is the resistance to electron transfer and R^{pro} is the resistance to ion transfer. R^{el} can be taken as a constant, but is generally difficult to predict. It is assumed that $R^{el} = 0.1\,\Omega\,cm^2$ in the present model.

The resistance to ion transfer can be calculated as

$$R^{pro} = \frac{H_m}{\kappa_m}. \tag{41}$$

(3) Concentration overpotential

The concentration overpotential of a PEMFC comprises of the anode and the cathode contributions, which can be calculated by

$$\eta_{conc} = -\frac{RT}{nF}\ln\left(1 - \frac{I}{I_L}\right), \tag{42}$$

where I_L is the limiting current density, and can be expressed as

$$I_L = \frac{nFD_k C_{k,0}}{H_d}. \tag{43}$$

Based on the above discussions, the cell voltage can be expressed as

$$V_{cell} = E - \eta_{act,a} - \eta_{act,c} - \eta_{ohm}^{el} - \eta_{ohm}^{pro} - \eta_{conc,a} - \eta_{conc,c}. \tag{44}$$

Table 1
Grid independence test ($I_{av} = 0.6\,A\,cm^{-2}$, $RH_c = 100\%$).

Stage	Grid size	V_{cell}, V
1	$32 \times 22 \times 64$	0.58554
	$42 \times 22 \times 64$	0.58556
	$52 \times 22 \times 64$	0.58558
2	$42 \times 12 \times 64$	0.58411
	$42 \times 22 \times 64$	0.58556
	$42 \times 34 \times 64$	0.58749
3	$42 \times 22 \times 44$	0.58549
	$42 \times 22 \times 64$	0.58556
	$42 \times 22 \times 74$	0.58559

Table 2
Parameters used in the model.

Parameter	Symbol	Value
Gas channel length	L	0.06 m
Gas channel width	W	1.0×10^{-3} m
Gas channel height	H_{ch}	1.0×10^{-3} m
Diffusion layer height	H_d	2.54×10^{-4} m
Catalyst layer height	H_{ct}	2.87×10^{-5} m
Membrane height	H_m	2.3×10^{-4} m
Land area width	W_{cc}	1.0×10^{-3} m
Faraday's constant	F	96487 C mol^{-1}
Operation temperature	T	353 K
Reference current density	I_{ref}	1 A cm^{-2}
Anode/cathode pressure	p_a/p_c	1/1 atm
Electron number of anode reaction	n_a	4
Electron number of cathode reaction	n_c	2
Fuel/air stoichiometric flow ratio	ζ_a/ζ_c	5/5
Relative humidity of inlet fuel	RH_a	100%
Oxygen mass fraction of inlet air	ω_o	0.23
H$_2$ diffusion coefficient at reference state	$D_{H_2,ref}$	0.915×10^{-4} m^2 s^{-1}
O$_2$ diffusion coefficient at reference state	$D_{O_2,ref}$	0.22×10^{-4} m^2 s^{-1}
Water vapor diffusion coefficient at reference state	$D_{w,ref}$	0.256×10^{-4} m^2 s^{-1}
Anode exchange current density multiply specific area	$A_s i_{a,ref}$	5.0×10^7 A m^{-3}
Cathode exchange current density multiply specific area	$A_s i_{c,ref}$	120 A m^{-3}
Hydrogen reference concentration	$C_{H_2,ref}$	56.4 mol m^{-3}
Oxygen reference concentration	$C_{O_2,ref}$	3.39 mol m^{-3}
Anode transfer coefficient	α_a	0.5
Cathode transfer coefficient	α_c	0.5
Porosity of diffusion layer	ε_d	0.3
Porosity of catalyst layer	ε_{ct}	0.28
Absolute permeability	K	1.76×10^{-11} m^2

3. Boundary conditions and numerical method

At the gas channel inlet, the temperature and species concentrations are assumed to be constant. The inlet velocities are specified by

$$u_{a,in} = \zeta_a \frac{I_{ref}}{2F} \frac{1}{C_{H_2,in}} \frac{A_m}{A_{ch}}, \tag{45}$$

$$u_{c,in} = \zeta_c \frac{I_{ref}}{4F} \frac{1}{c_{O_2,in}} \frac{A_m}{A_{ch}}, \tag{46}$$

where ζ_a and ζ_c are the reactant stoichiometric flow ratio of anode and cathode, respectively, A_m is the geometrical area of the membrane, and A_{ch} is the cross-sectional area of the gas channel.

In the x–z planes, the symmetrical conditions are adopted, i.e., the gradient in the y-direction of each variable is zero.

A local one-way assumption is adopted to provide the channel outlet velocity condition, and is then corrected using global mass conservation constraint [20].

At the body surface, the no-slip condition is applied for the velocity and the non-permeable condition is applied for the species mass fraction.

For the liquid water saturation, the computational domain involves two diffusion layers, two catalyst layers and a membrane. At the diffusion layer and gas channel interface, the water saturation is zero [11], and at the diffusion layer and current collector land interface, the gradient in z-direction is zero, i.e., $\partial s/\partial z = 0$.

The governing equations and the boundary conditions are discretized using the finite volume method. The SIMPLEC algorithm [20] is used for coupling of the velocity and pressure. Since all governing equations are coupled to one another, they should be solved simultaneously using an iterative method. The solution is considered to be convergent when the relative error for each dependent variable between two consecutive iterations is less than 1.0×10^{-5}.

To simulate local transport phenomena in the fuel cell, the grid arrangement in the z-direction is non-uniform. A grid independence test was carried out for nine grid systems. Cell voltage results computed using the model under different grid systems for $I_{av} = 0.6\,A\,cm^{-2}$ and $RH_c = 100\%$ are summarized in Table 1. Considering both accuracy and economics, the grid system of $42 \times 22 \times 64$ was selected for the present study.

The parameters used in the present model are listed in Table 2.

4. Results and discussion

4.1. Model validation

The predicted fuel cell polarization curve of the PEMFC is shown in Fig. 2. Provided there are also the experimental data of Ticianelli et al. [21], from which the major operation parameters are adopted. The predicted curve shows good agreement with the experimental data at lower current density. While at high current density ($I_{av} > 0.8\,A\,cm^{-2}$), there is some difference between the predicted

results and the experimental data, with the predicted value being higher than that of measured. It is probably due to the model that cannot fully illuminate the effect of liquid water on PEMFC performance. At high current density, a significant amount of water is produced at the cathode that may lead to water flooding. In the present model, the liquid water is taken as a parameter, liquid water saturation, which denotes the ratio of the liquid volume to the pore volume. This definition can analysis the effect of liquid water on the PEMFC performance to some extend, but cannot fully reveal the water flooding at the cathode, and hence the present model overestimates the cell performance. However, the present two-phase model can still provide some useful information for further understanding the complicated process of the PEMFC. The development
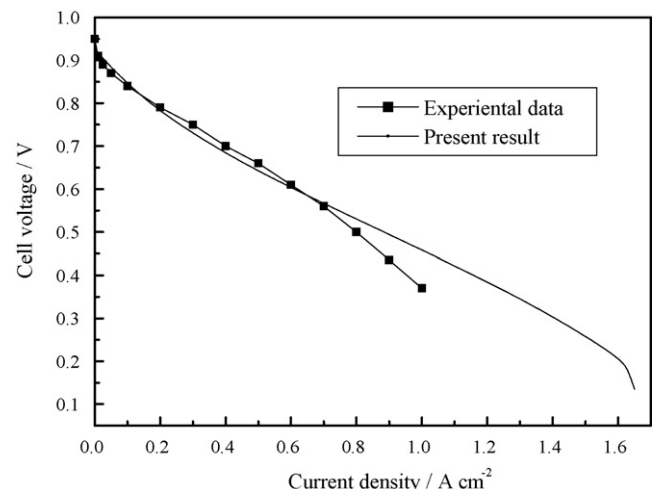
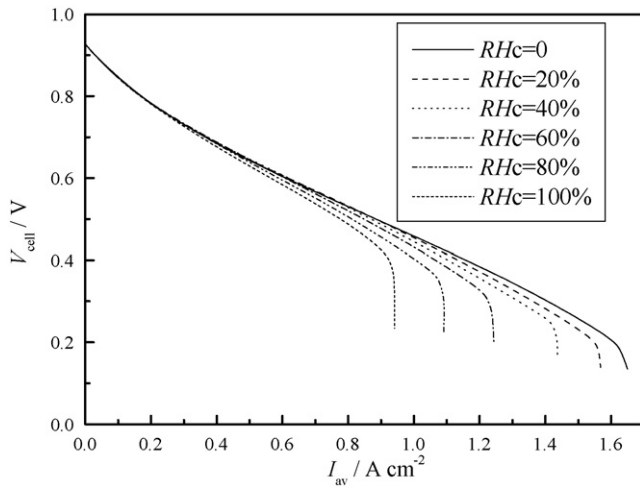**Fig. 2.** Comparison of present model results to experimental data.

Fig. 3. Effect of the cathode humidity on the cell performance.

Fig. 5. Liquid water saturation distribution in the cathode diffusion and catalyst layers ($RH_c = 80\%$, $I_{av} = 0.9\,A\,cm^{-2}$).

of a detailed two-phase model for liquid water drop transport will be analyzed in our future work.

4.2. Effect of the cathode humidity on PEMFC performance

Fig. 3 shows the effect of the cathode humidity on PEMFC performance. It can be seen that the lower humidity is beneficial in improving the cell performance. This phenomenon can be explained by the oxygen concentration distribution at the cathode electrode/membrane interface (see Fig. 4). It can be found that the oxygen concentration for $RH_c = 0$ is much higher than that for $RH_c = 80\%$ which results in the different PEMFC performances.

It should be noted that different researchers presented different results about the effect of cathode humidity on PEMFC performance. For instance, the experimental results given by Santarelli and Torchio [22] are fully adverse to our present work. However, the numerical results given by Natarajan and Nguyen [23] are similar to our present work although different from some experiments. They considered that the experiments are conducted under conditions are the anode is not properly humidified and hence any increase in the cathode humidity improves the hydration levels of the membrane and the PEMFC performance. The numerical results given by Um and Wang [24] have the similar trend to the experiments of Ref. [22]. Lee and Chu [25] and Wang et al. [26] reported that at low-operating voltage, the cell performance decreases with
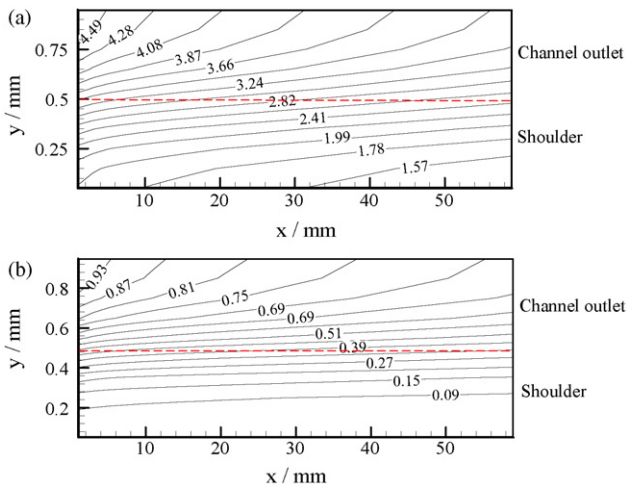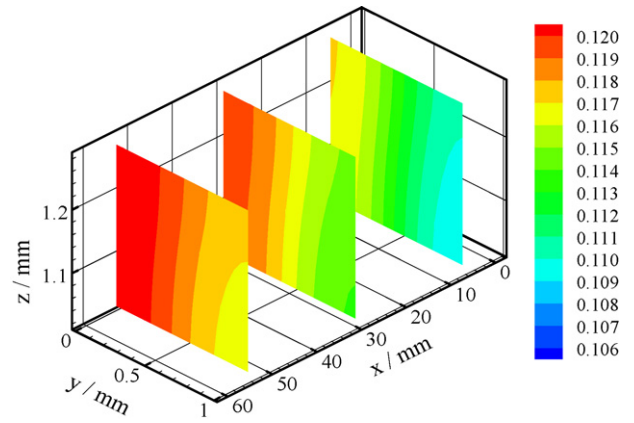
RH_c, and as the operating voltage increases, the effect of RH_c on cell performance reverses.

Based on the above analysis, the author is fully aware that the reliable test data are extremely important to validate a numerical model. Furthermore, the fuel cell researchers can improve the present model or develop new models to accelerate the process. Some suggestions have been presented in our previous work [9].

4.3. Distribution of water saturation

In this section, the liquid water saturation distribution in the cathode diffusion and catalyst layers for $RH_c = 80\%$ is first shown in Fig. 5. The results show that the water saturation increases along the channel since the electrochemical reaction takes place in the catalyst layer. Water removal in front of the shoulder is transported to the channel first, and hence the saturation in this region is greater than that in the region in front of the channel.

It can be obviously seen that the water saturation distribution in the cathode electrode has an identical trend with the public literatures, such as Ref. [5]. Hence, the present study mainly focuses on the water saturation distribution in the anode electrode, which is often ignored in the public literatures.

Generally, the humidified hydrogen is fed into the anode channel. As is known, $\omega_w + \omega_{H_2} = 1$ in the whole anode region since the anode gas stream is a binary mixture. Hence the relative ratio, $f = (\omega_{w,out}/\omega_{H_2,out})/(\omega_{w,in}/\omega_{H_2,in})$, denotes the relative consumption rate of hydrogen and transport of water vapor. $f > 1$ means the hydrogen consumption rate is higher than the water vapor transport and leads to the water vapor condensation along the channel, as reported in Ref. [27]. Generally speaking, the liquid water at the anode is caused by diffusion through membrane from the cathode side due to the water concentration gradient. However, in the following sections of the present work, it is found that the liquid water can also be generated by condensation.

The value of f depends not only on the anode inlet humidity but also on the net water transport coefficient per proton. The net water transport coefficient per proton at various current densities is shown in Fig. 6. It follows the variation trend observed for the PEMFC in Ref. [28], i.e., the net water transport coefficient per proton decreases sharply with current density, but it reaches a nearly constant value when $I_{av} > 0.6\,A\,cm^{-2}$. The reason is that the flows of protons and water from the anode to cathode increase linearly with current density. At the same time, the back-diffused water from the cathode to anode increases since the generated water at the cathode catalyst layer by oxygen reduction reaction (ORR) increases linearly with current density. It can be concluded that it is easy to get oversaturated water vapor at the anode at high current den-
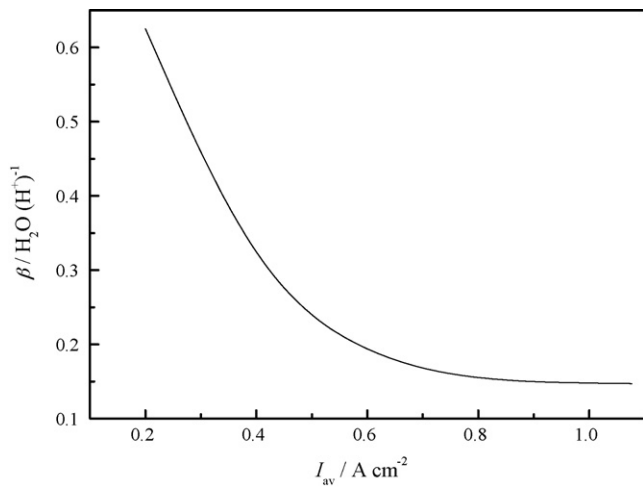

Fig. 4. Oxygen molar concentration distribution: (a) $RH_c = 0$ and (b) $RH_c = 80\%$.

Fig. 6. Net water transport coefficients per proton at various current densities ($RH_c = 80\%$).

sity, when the water vapor transport is lower than the hydrogen consumption rate.

Fig. 7 shows the liquid water saturation distribution in the anode diffusion and catalyst layers for $RH_c = 80\%$. It can be seen that the liquid water is generated because the water vapor transport is less than the hydrogen consumption rate. With the decrease of current density, the net water transport coefficient per proton increases and as a result, the water saturation decreases. In fact, the computational results show that the water vapor will not condense when $I_{av} < 0.4\,A\,cm^{-2}$.
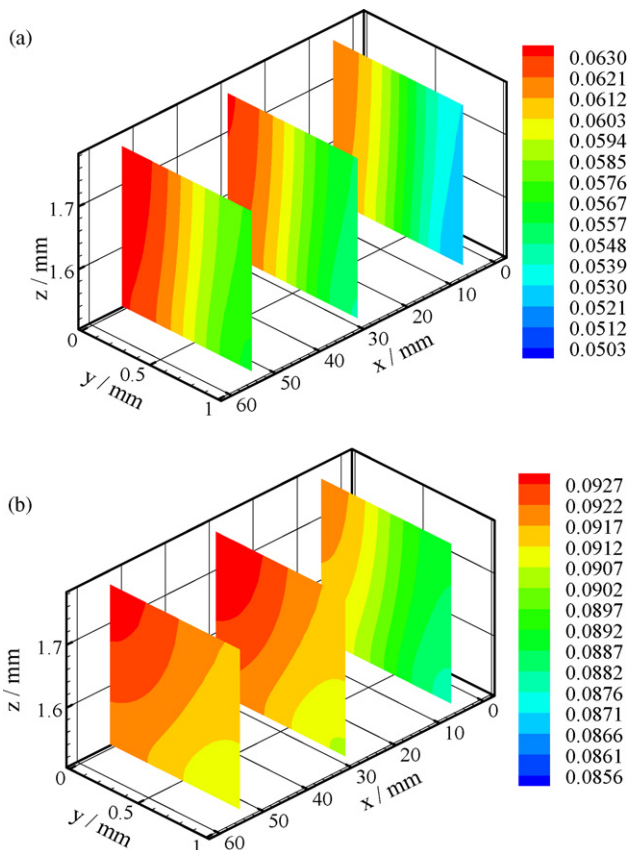

Fig. 7. Water saturation distribution in the anode diffusion and catalyst layers for $RH_c = 80\%$: (a) $I_{av} = 0.6\,A\,cm^{-2}$ and (b) $I_{av} = 0.9\,A\,cm^{-2}$.
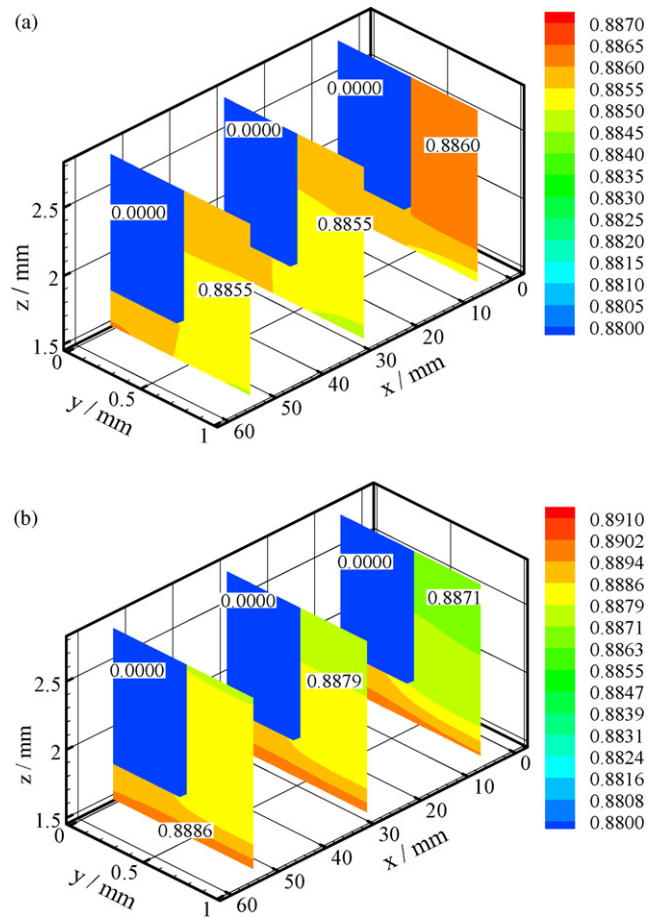

Fig. 8. Water vapor mass fraction distribution in the anode diffusion and catalyst layers for $RH_c = 80\%$: (a) $I_{av} = 0.6\,A\,cm^{-2}$ and (b) $I_{av} = 0.9\,A\,cm^{-2}$.

The above results can also be explained by the water vapor concentration distribution in the anode diffusion and catalyst layers (see Fig. 8). At high current density, the water vapor concentration increases along the channel, and hence the water vapor is condensed. Conversely, the water vapor concentration decreases along the channel at low current density, which will not lead to the water vapor condensation.

4.4. Distribution of temperature

Fig. 9 shows the distribution of the reactant fluid temperature at $I_{av} = 0.9\,A\,cm^{-2}$. It can be found that the temperature peak appears in the cathode catalyst layer, implying that the heat generation takes place in this region due to the reversible and irreversible entropy productions. Fig. 10 shows the temperature difference between the solid matrix and reactant fluid in the cathode gas diffusion layer. Near the catalyst layer, the reactant fluid temperature is higher than the solid matrix temperature. Whereas, far from the catalyst layer the temperature difference between the gas mixture and solid matrix decreases. Near the channel, the reactant fluid temperature is lower than the solid matrix temperature. The reason can be explained as follows. The solid matrix is like a fin. Near to the catalyst layer, the fluid temperature is relatively higher due to the generated heat by the electrochemical reaction. The solid matrix is heated by the heat fluid and the condensation occurs, and hence the fluid temperature is higher than the solid matrix temperature. Near the channel, the fluid temperature is relative lower and the solid matrix is cooled by the fluid, and hence the temperature difference between the fluid and solid matrix reverses.
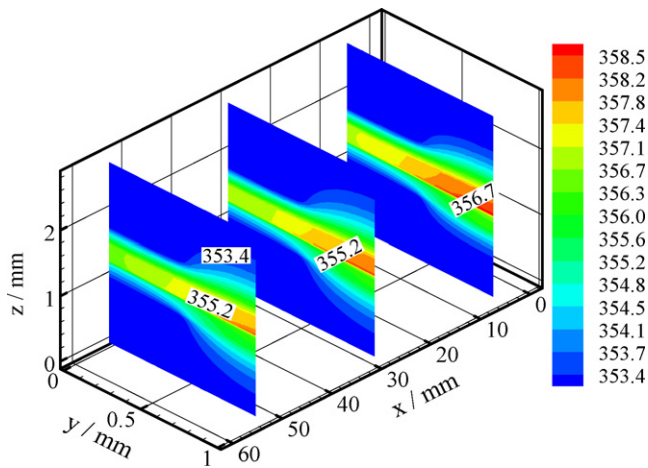
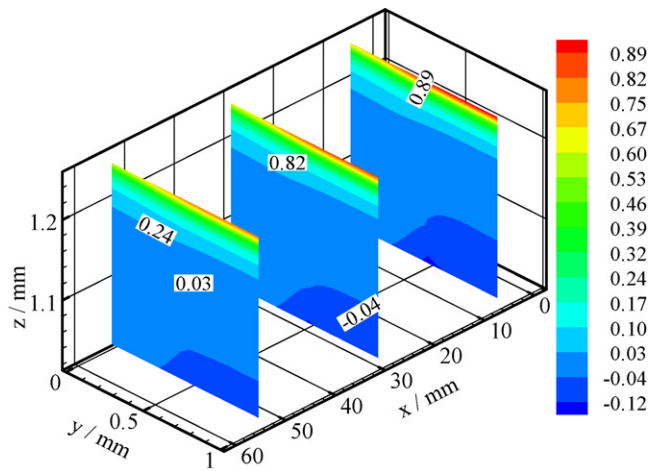**Fig. 9.** Reactant fluid temperature distribution in the cell ($I_{av} = 0.9\,A\,cm^{-2}$, $RH_c = 80\%$).

Fig. 10. Temperature difference between the solid matrix and gas mixture ($I_{av} = 0.9\,A\,cm^{-2}$, $RH_c = 80\%$).

5. Conclusions

In this paper, a three-dimensional, two-phase and non-isothermal PEMFC model based on the previously developed model was established using the two-fluid method. The main conclusions are:

(1) The oxygen concentration at the cathode for $RH_c = 0$ is much higher than that for $RH_c = 80\%$, and the lower cathode humidity is beneficial for cell performance.
(2) The liquid water saturation increases along the channel in the cathode electrode. The water vapor at the anode can be condensed at high current density because the water vapor transport is less than the hydrogen consumption rate.
(3) The temperature peak appears in the cathode catalyst layer. Near the catalyst layer, the reactant fluid temperature is higher than the solid matrix temperature. Far from the catalyst layer, the temperature difference between the reactant fluid and solid matrix decreases. Near the channel, the reactant fluid temperature is lower than the solid matrix temperature.

References

[1] W. He, J.S. Yi, T.V. Nguyen, AIChE J. 46 (2000) 2053–2064.
[2] N.P. Siegel, M.W. Ellis, D.J. Nelson, M.R. von Spakovsky, J. Power Sources 128 (2004) 173–184.
[3] L. You, H. Liu, Int. J. Heat Mass Transfer 45 (2002) 2277–2287.
[4] H. Sun, H. Liu, L.J. Guo, J. Power Sources 143 (2005) 125–135.
[5] G. Hu, J. Fan, Energy Fuels 20 (2006) 738–747.
[6] Z.H. Wang, C.Y. Wang, K.S. Chen, J. Power Sources 94 (2001) 40–50.
[7] F.L. Chen, M.H. Chang, P.T. Hsieh, Int. J. Hydrogen Energy 33 (2008) 2525–2529.
[8] W.Q. Tao, C.H. Min, X.L. Liu, Y.L. He, B.H. Yin, W. Jiang, J. Power Sources 160 (2006) 359–373.
[9] C.H. Min, Y.L. He, X.L. Liu, B.H. Yin, W. Jiang, W.Q. Tao, J. Power Sources 160 (2006) 374–385.
[10] G.L. He, P. Ming, Z. Zhao, A. Abudula, Y. Xiao, J. Power Sources 163 (2007) 864–873.
[11] H. Meng, J. Power Sources 168 (2007) 218–228.
[12] X. Liu, H. Guo, F. Ye, C.F. Ma, Electrochim. Acta 52 (2007) 2607–3614.
[13] C.H. Min, J. Power Sources 186 (2009) 370–376.
[14] D. Natarajan, T.V. Nguyen, J. Electrochem. Soc. 148 (2001) A1324–A1335.
[15] J.J. Hwang, J. Power Sources 164 (2007) 174–181.
[16] T. Berning, D.M. Lu, N. Djilali, J. Power Sources 106 (2002) 284–294.
[17] J.R. Fan, G.L. Hu, J. Yao, K.F. Cen, Energy Fuels 16 (2002) 1591–1598.
[18] W. Ying, T.H. Yang, W.Y. Lee, J. Ke, C.S. Kim, J. Power Sources 145 (2005) 572–581.
[19] K.W. Lum, J.J. McGuirk, J. Power Sources 143 (2005) 103–124.
[20] W.Q. Tao, Numerical Heat Transfer, 2nd ed., Xi'an Jiaotong University Press, Xi'an, 2001, p. 220.
[21] E.A. Ticianelli, C.R. Derouin, S. Srinivasan, J. Electroanal. Chem. 251 (1988) 275–295.
[22] M.G. Santarelli, M.F. Torchio, Energy Convers. Manage. 48 (2007) 40–51.
[23] D. Natarajan, T.V. Nguyen, J. Power Sources 115 (2003) 66–80.
[24] S. Um, C.Y. Wang, J. Power Sources 156 (2006) 211–223.
[25] C.I. Lee, H.S. Chu, J. Power Sources 161 (2006) 949–956.
[26] X.D. Wang, Y.Y. Duan, W.M. Yan, F.B. Weng, J. Power Sources 176 (2008) 247–258.
[27] F. Liu, G. Lu, C.Y. Wang, J. Membr. Sci. 287 (2007) 126–131.
[28] Q. Yan, H. Toghiani, J. Wu, J. Power Sources 158 (2006) 316–325.